PHYSICAL REVIEW B **107**, 045138 (2023)

Unprotected edge modes in quantum spin Hall insulator candidate materials

Nguyen Minh Nguyen,[1] Giuseppe Cuono,[1] Rajibul Islam,[1] Carmine Autieri,[1,2,*]
Timo Hyart,[3,4,1,†] and Wojciech Brzezicki[1,5,‡]
[1]*International Research Centre MagTop, Institute of Physics, Polish Academy of Sciences, Aleja Lotników 32/46, PL-02668 Warsaw, Poland*
[2]*Consiglio Nazionale delle Ricerche CNR-SPIN, UOS Salerno, I-84084 Fisciano (Salerno), Italy*
[3]*Computational Physics Laboratory, Physics Unit, Faculty of Engineering and Natural Sciences,*
Tampere University, FI-33014 Tampere, Finland
[4]*Department of Applied Physics, Aalto University, FI-00076 Aalto, Espoo, Finland*
[5]*Institute of Theoretical Physics, Jagiellonian University, ulica S. Łojasiewicza 11, PL-30348 Kraków, Poland*

(Received 20 September 2022; revised 13 December 2022; accepted 13 January 2023; published 26 January 2023)

The experiments in quantum spin Hall insulator candidate materials, such as HgTe/CdTe and InAs/GaSb heterostructures, indicate that in addition to the topologically protected helical edge modes, these multilayer heterostructures may also support additional edge states, which can contribute to scattering and transport. We use first-principles calculations to derive an effective tight-binding model for HgTe/CdTe, HgS/CdTe, and InAs/GaSb heterostructures, and we show that all these materials support additional edge states which are sensitive to edge termination. We trace the microscopic origin of these states back to a minimal model supporting flat bands with a nontrivial quantum geometry that gives rise to polarization charges at the edges. We show that the polarization charges transform into additional edge states when the flat bands are coupled to each other and to the other states to form the Hamiltonian describing the full heterostructure. Interestingly, in HgTe/CdTe quantum wells the additional edge states are far away from the Fermi level so that they do not contribute to the transport, but in the HgS/CdTe and InAs/GaSb heterostructures they appear within the bulk energy gap, giving rise to the possibility of multimode edge transport. Finally, we demonstrate that because these additional edge modes are nontopological it is possible to remove them from the bulk energy gap by modifying the edge potential, for example, with the help of a side gate or chemical doping.

DOI: 10.1103/PhysRevB.107.045138

I. INTRODUCTION

The theory of the quantum spin Hall (QSH) effect predicts the existence of helical edge modes, which are topologically protected against elastic backscattering from all perturbations obeying time-reversal symmetry, and various materials have been predicted to support the QSH insulator phase [1–4]. Experimentally, signatures of edge mode transport have been observed in several of the candidate materials such as HgTe/CdTe quantum wells [5], InAs/GaSb bilayers [6], and WTe_2 [7]. However, experimental studies have also led to discrepancies with the simple theoretical models. In WTe_2 the protection length of the edge transport is only a few tens of nanometers [7], and even in the more extensively studied InAs/GaSb and HgTe/CdTe quantum wells the best protection lengths reached so far are on the order of a few micrometers [6] and a few tens of micrometers [8], respectively. There is still no consensus about the interpretation of the observed short protection lengths but various mechanisms, such as magnetic impurities [9], phonons [10], dynamic nuclear polarization [11,12], spontaneous time-reversal symmetry breaking [13,14], charge puddles [15], charge dopants [16], and interaction effects [17], may contribute to the breakdown of topological protection.

The quality of the edge transport can be improved with the help of impurity doping in InAs/GaSb bilayers [6] and gate training in HgTe/CdTe quantum wells [8], indicating that there likely exist some additional unprotected low-energy states, which are contributing to the breakdown of the topological protection and which are influenced by these sample preparation techniques. In certain experiments unprotected edge states have been observed also more directly. Namely, in InAs/GaSb bilayers, in the absence of impurity doping, multimode edge transport has been experimentally observed in the trivial regime [18]. In HgTe/CdTe quantum wells the additional states seem to be sufficiently far away from the Fermi level so that they do not contribute to transport, but the dynamical properties suggest that the topological edge states are surrounded by additional states contributing to scattering [19]. The microscopic origin of these additional states remains unknown in both materials.

In this paper, we use first-principles calculations to derive an effective tight-binding model for HgTe/CdTe, HgS/CdTe, and InAs/GaSb heterostructures, and we show that all these materials support additional edge states which are sensitive to the edge termination. We trace the microscopic origin of these states back to a minimal model of a buckled honeycomb

---

[*] autieri@magtop.ifpan.edu.pl
[†] timo.hyart@tuni.fi
[‡] brzezicki@magtop.ifpan.edu.pl

TABLE I. Tight-binding parameters (in eV) of different materials.

Parameters	HgTe	HgS	CdTe	InAs	GaSb	AlSb
V_{s_a}	−5.8329	−12.1315	−6.1832	−7.8000	−5.4804	−4.2606
V_{s_c}	0.2069	−1.5535	1.6395	−3.5834	−5.5334	−3.0847
V_{p_a}	3.1483	−1.1909	2.3251	−0.1424	−0.2514	0.4210
V_{p_c}	7.6916	5.4898	7.4584	4.1314	2.8382	3.9110
$V_{ss\sigma}$	−1.2569	−0.1162	−1.2431	−0.1424	−0.2514	0.4210
$V_{s_a p_c \sigma}$	1.7229	2.8306	1.6379	−1.4257	−1.5325	−1.6150
$V_{s_c p_a \sigma}$	1.4834	1.1517	1.5463	1.4669	1.2761	1.3486
$V_{pp\sigma}$	2.2132	1.5759	2.0139	2.2223	2.200	2.0384
$V_{pp\pi}$	−0.9830	−0.4231	−0.9875	−1.1509	−1.1513	−1.1146
λ_a	0.3943/2	−0.0159/2	0.5350/2	0.2083/2	0.4423/2	0.4237/2
λ_c	0.7216/2	0.7651/2	0.1950/2	0.2856/2	0.1246/2	0.0306/2
E_f	3.32248	−1.33027	3.32331	0.173742	0.293268	1.71368

lattice of anions and cations. This system is the minimal building block for constructing HgTe/CdTe, HgS/CdTe, and InAs/GaSb heterostructures, and it supports flat bands with nontrivial quantum geometry that gives rise to polarization charges at the edges [20]. We show that the polarization charges transform into additional edge states when the flat bands are coupled to each other and to the other states to form the Hamiltonian describing the full heterostructure. In HgTe/CdTe quantum wells the additional edge states are far away from the Fermi level so that they do not contribute to the transport, but in the HgS/CdTe and InAs/GaSb heterostructures they appear within the bulk energy gap, giving rise to the possibility of multimode edge transport, in agreement with experiments [18,19]. Finally, we demonstrate that because these additional edge modes are nontopological, it is possible to remove them from the bulk energy gap by modifying the edge potential, for example, with the help of a side gate or chemical doping, providing a possible explanation for the mysterious improvement of the quality of the QSH effect with the help of impurity doping in InAs/GaSb bilayers [6] and gate training in HgTe/CdTe quantum wells [8]. We note that trivial helical states were also reported in a recent theoretical work on InAs/GaSb heterostructures [21].

II. HETEROSTRUCTURE HAMILTONIAN AND NONTOPOLOGICAL EDGE STATES

Our starting point are the Hamiltonians for HgTe, HgS, CdTe, InAs, GaSb, and AlSb bulk crystals,

$$
\begin{aligned}
\mathcal{H}(\mathbf{k}) = {} & \mathbb{1}_2 \otimes h_A \otimes \begin{pmatrix} 0 & e^{ik_3} \\ 0 & 0 \end{pmatrix} + \mathbb{1}_2 \otimes h_B \otimes \begin{pmatrix} 0 & e^{ik_1} \\ 0 & 0 \end{pmatrix} + \mathbb{1}_2 \otimes h_C \otimes \begin{pmatrix} 0 & 1 \\ 0 & 0 \end{pmatrix} + \mathbb{1}_2 \otimes h_D \otimes \begin{pmatrix} 0 & e^{i(k_3-k_2)} \\ 0 & 0 \end{pmatrix} + \text{H.c.} \\
& + \mathbb{1}_2 \otimes E_c \otimes \begin{pmatrix} 1 & 0 \\ 0 & 0 \end{pmatrix} + \mathbb{1}_2 \otimes E_a \otimes \begin{pmatrix} 0 & 0 \\ 0 & 1 \end{pmatrix} - \sum_{\alpha=1,2,3} \sigma_\alpha \otimes L_\alpha \otimes \begin{pmatrix} \lambda_c & 0 \\ 0 & \lambda_a \end{pmatrix} - E_f \otimes \mathbb{1}_{16},
\end{aligned} \tag{1}
$$

$$
h_A = h\left(\frac{1}{\sqrt{3}}, \frac{1}{\sqrt{3}}, \frac{1}{\sqrt{3}}\right), \quad h_B = h\left(\frac{1}{\sqrt{3}}, -\frac{1}{\sqrt{3}}, -\frac{1}{\sqrt{3}}\right), \quad h_C = h\left(-\frac{1}{\sqrt{3}}, \frac{1}{\sqrt{3}}, -\frac{1}{\sqrt{3}}\right), \quad h_D = h\left(-\frac{1}{\sqrt{3}}, -\frac{1}{\sqrt{3}}, \frac{1}{\sqrt{3}}\right), \tag{2}
$$

$$
h(l,m,n) = \begin{pmatrix} V_{ss\sigma} & lV_{s_c p_a \sigma} & mV_{s_c p_a \sigma} & nV_{s_c p_a \sigma} \\ -lV_{s_a p_c \sigma} & l^2(V_{pp\sigma} - V_{pp\pi}) + V_{pp\pi} & lm(-V_{pp\pi} + V_{pp\sigma}) & ln(-V_{pp\pi} + V_{pp\sigma}) \\ -mV_{s_a p_c \sigma} & lm(-V_{pp\pi} + V_{pp\sigma}) & m^2(V_{pp\sigma} - V_{pp\pi}) + V_{pp\pi} & mn(-V_{pp\pi} + V_{pp\sigma}) \\ -nV_{s_a p_c \sigma} & ln(-V_{pp\pi} + V_{pp\sigma}) & mn(-V_{pp\pi} + V_{pp\sigma}) & n^2(V_{pp\sigma} - V_{pp\pi}) + V_{pp\pi} \end{pmatrix}, \tag{3}
$$

$$
L_x = i\begin{pmatrix} 0 & 0 & 0 & 0 \\ 0 & 0 & 1 & 0 \\ 0 & -1 & 0 & 0 \\ 0 & 0 & 0 & 0 \end{pmatrix}, \;
L_y = i\begin{pmatrix} 0 & 0 & 0 & 0 \\ 0 & 0 & 0 & -1 \\ 0 & 0 & 0 & 0 \\ 0 & 1 & 0 & 0 \end{pmatrix}, \;
L_z = i\begin{pmatrix} 0 & 0 & 0 & 0 \\ 0 & 0 & 0 & 0 \\ 0 & 0 & 0 & 1 \\ 0 & 0 & -1 & 0 \end{pmatrix}, \;
E_{a(c)} = \begin{pmatrix} V_{s_{a(c)}} & 0 & 0 & 0 \\ 0 & V_{p_{a(c)}} & 0 & 0 \\ 0 & 0 & V_{p_{a(c)}} & 0 \\ 0 & 0 & 0 & V_{p_{a(c)}} \end{pmatrix}, \tag{4}
$$

where the tight-binding parameters for each material, given in Table I, have been derived from first-principles density-functional theory (DFT) calculations. To obtain the tight-binding with first-neighbor hopping parameters, we impose to the tight-binding model to fit the DFT band structure at the high-symmetry points extracting the on-site energies, the hopping amplitudes, and the spin-orbit couplings as fitting parameters. More technical information is provided in Appendixes A and B. Here, the unit cell of the zinc-blende crystal structure contains two lattice sites, anions and cations, at positions (0,0,0) and (1/2, 1/2, 1/2) with lattice translation vectors being $\mathbf{n}_1 = (1, 1, 0)$, $\mathbf{n}_2 = (-1, 1, 0)$, and

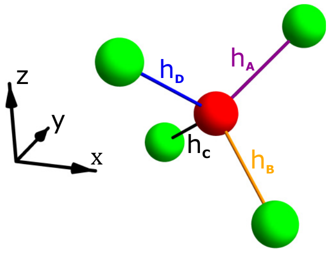

FIG. 1. Schematic illustration of the hopping matrices h_α ($\alpha = A, B, C, D$) between the nearest-neighbor lattice sites in zinc-blende crystals. Each cation (green) and anion (red) supports one s orbital and three p orbitals so that h_i are 4×4 matrices.

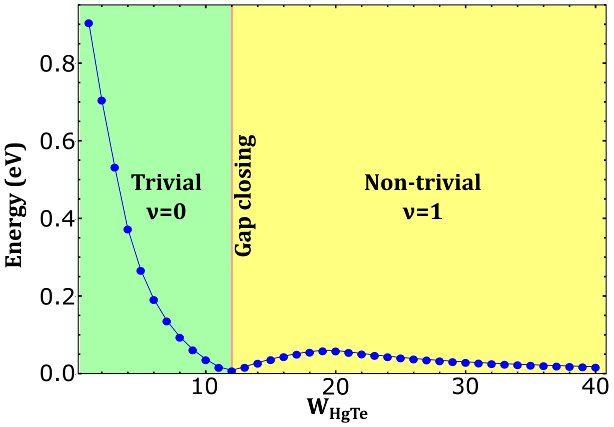

FIG. 2. Energy gap E_{gap} and topological invariant ν as a function of the quantum well thickness W_{HgTe} in a $\text{CdTe}_{10}/\text{HgTe}_{W_{\text{HgTe}}}/\text{CdTe}_{10}$ heterostructure. The transition from the topologically trivial $\nu = 0$ to nontrivial $\nu = 1$ phase takes place at $W_{\text{HgTe,c}} = 12$ unit cells.

$\mathbf{n}_3 = (0, 1, 1)$. Each site in the unit cell supports one s orbital and three p orbitals, h_α are 4×4 matrices describing the hopping amplitudes between the different orbitals of cations and anions [parametrized by $V_{ss\sigma}, V_{s_a p_c \sigma}, V_{s_c p_a \sigma}, V_{pp\sigma}$, and $V_{pp\pi}$ in Eq. (3)] along the different directions $\alpha = A, B, C, D$ as depicted in Fig. 1, matrices $E_{a(c)}$ contain the on-site energies $V_{s_{a(c)}}$ and $V_{p_{a(c)}}$ of the s and p orbitals of the anions (cations), σ_α are Pauli spin matrices, L_α are the 4×4 angular momentum matrices, $\lambda_{a(c)}$ is the spin-orbit coupling strength at the anion (cation) site, and E_f is the Fermi energy.

The two-dimensional (2D) Hamiltonian $\mathcal{H}^{2\text{D}}(k_1, k_2)$ of a quantum heterostructure $X_{W_X}/Y_{W_Y}/X_{W_X}$, consisting of W_X unit cells of material X (insulating barrier), W_Y unit cells of material Y (quantum well), and W_X unit cells of material X (insulating barrier), stacked along the $\mathbf{n}_3$ direction, can be written as

$$\mathcal{H}^{2\text{D}}(k_1, k_2) = \sum_i |i\rangle\langle i| \otimes H_0(k_1, k_2, i) + \left(\sum_i |i\rangle\langle i+1| \otimes H_1(k_1, k_2, i) + \text{H.c.}\right), \tag{5}$$

where $|i\rangle$ is the basis state for the ith unit cell along the $\mathbf{n}_3$ direction, and

$$H_0(k_1, k_2, i) = \begin{cases} H_0^X, & 0 < i \leqslant W_X, \\ H_0^y, & W_X < i \leqslant W_X + W_Y, \\ H_0^X, & W_X + W_Y < i \leqslant 2W_X + W_Y, \end{cases} \tag{6}$$

$$H_1(k_1, k_2, i) = \begin{cases} H_1^X, & 0 < i < W_X, \\ H_1^{XY}, & i = W_X, \\ H_1^y, & W_X < i < W_X + W_Y, \\ H_1^{XY}, & i = W_X + W_Y, \\ H_1^X, & W_X + W_Y < i \leqslant 2W_X + W_Y, \end{cases} \tag{7}$$

with $H_0^X(k_1, k_2)$ and $H_1^X(k_1, k_2)$ obtained from the Fourier decomposition of $\mathcal{H}(\mathbf{k})$ [Eq. (1)] of material X,

$$\mathcal{H}(\mathbf{k}) = H_0(k_1, k_2) + e^{ik_3} H_1(k_1, k_2) + e^{-ik_3} H_1^\dagger(k_1, k_2). \tag{8}$$

We assume that the hopping matrices between the different materials H_1^{XY} can be written as

$$H_1^{XY} = (1 - x)\frac{H_1^X + H_1^y}{2}, \tag{9}$$

allowing us to turn the coupling between the materials on and off by changing x continuously from 0 to 1. This is useful in the following when we study the microscopic origin of the nontopological edge modes. If not otherwise stated we use $x = 0$ so that the coupling is turned on. We have benchmarked the tight-binding model by studying the topological phase transition in CdTe/HgTe/CdTe quantum wells. As shown in Fig. 2 we obtain a transition from a topologically trivial to nontrivial phase at $W_{\text{HgTe},c} = 12$ unit cells in approximate agreement with previous studies [2,3].

To study the edge state spectra of these materials we consider one-dimensional ribbons of width W' along the $\mathbf{n}_2$ direction,

$$\mathcal{H}^{1\text{D}}(k_1) = \mathbb{1}_{W'} \otimes H_0'(k_1) + D \otimes H_1'(k_1) + D^\intercal \otimes H_1'^\dagger(k_1), \tag{10}$$

where

$$D = \sum_{i=1}^{W'-1} |i\rangle\langle i+1|, \tag{11}$$

and $H_0'(k_1)$ and $H_1'(k_1)$ are obtained from the Fourier decomposition

$$\mathcal{H}^{2\text{D}}(k_1, k_2) = H_0'(k_1) + e^{ik_2} H_1'(k_1) + e^{-ik_2} H_1'^\dagger(k_1). \tag{12}$$

Based on previous studies we expect that CdTe/HgTe/CdTe quantum wells support a pair of counterpropagating helical edge states connecting through the bulk gap in the topologically nontrivial regime $W_{\text{HgTe}} > W_{\text{HgTe},c}$ [2,3,5], whereas we expect that there are no edge states in the trivial regime $W_{\text{HgTe}} < W_{\text{HgTe},c}$. However, we find that the spectra of CdTe/HgTe/CdTe and CdTe/HgS/CdTe compounds support additional edge states as shown in Figs. 3 and 4, respectively. In the case of CdTe/HgTe/CdTe, the additional edge states appear at energies far away from the bulk gap so that they do not contribute to the transport, but in CdTe/HgS/CdTe the edge states are observed inside the bulk gap, giving rise to the possibility of multimode edge transport. We find that these additional edge states can appear in nontrivial and trivial heterostructures, and in Fig. 4 we also demonstrate that

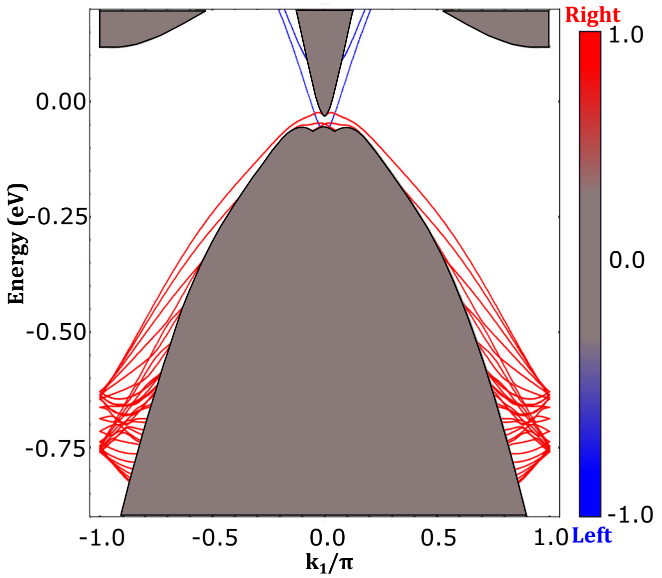

FIG. 3. Edge state spectrum of a topologically nontrivial $\mathrm{CdTe}_{10}/\mathrm{HgTe}_{16}/\mathrm{CdTe}_{10}$ heterostructure with width $W' = 300$ unit cells. The colors (normalized to maximum absolute values) indicate the projection of the eigenstates onto 20 unit cells located at the left (blue) and right (red) edges of the system. Two pairs of topological helical edge states connect the conduction and valence band through the bulk gap. Additionally, there exists a large number of nontopological edge states far away from the Fermi level.

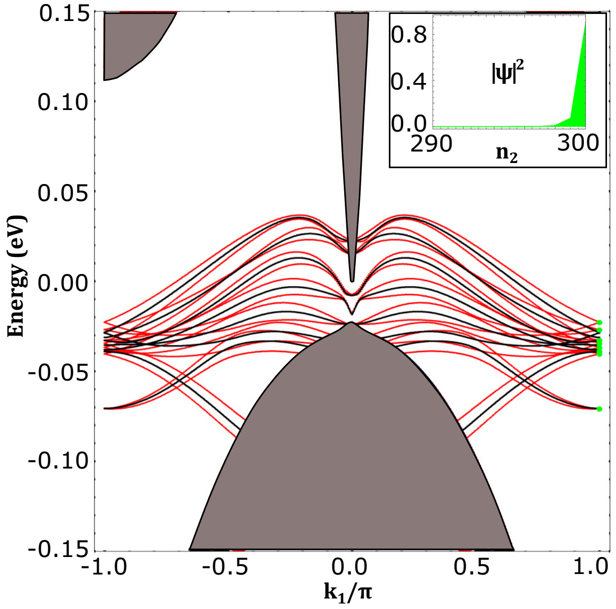

FIG. 4. Edge state spectrum of a topologically trivial $\mathrm{CdTe}_{10}/\mathrm{HgS}_{8}/\mathrm{CdTe}_{10}$ heterostructure with width $W' = 300$ unit cells. In the presence of spin-orbit coupling we have used the same colors as in Fig. 3 (states localized at the right edge are red), whereas in the absence of spin-orbit coupling ($\lambda_{1,2} = 0$) the projection on the right-hand side is indicated with black. Inset: Local density of states (LDOS) as a function of position $\mathbf{n}_2$ close to the right edge for the edge states at $k_1 = \pi$ (green dots).

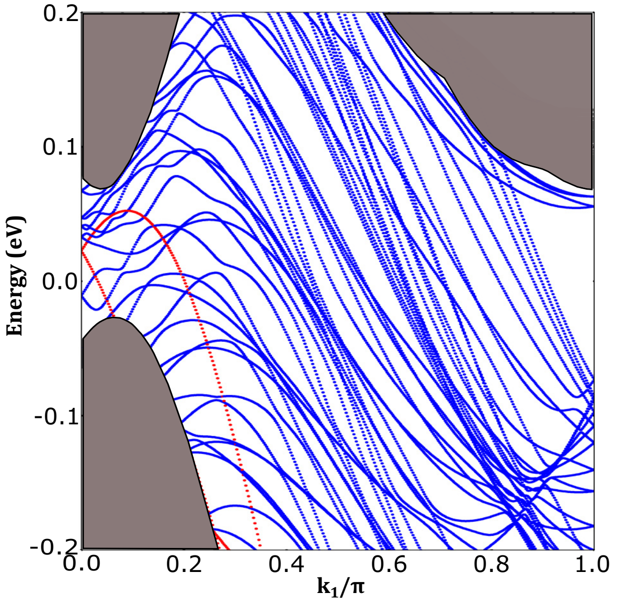

FIG. 5. Edge state spectrum of a topologically trivial $\mathrm{AlSb}_{10}/\mathrm{InAs}_{10}/\mathrm{GaSb}_{10}/\mathrm{AlSb}_{10}$ heterostructure with width $W' = 300$ unit cells.

spin-orbit coupling does not play a significant role in the appearance of nontopological edge states. Finally, in Fig. 5 we demonstrate that this type of nontopological edge states appear also in topologically trivial AlSb/InAs/GaSb/AlSb heterostructures inside the bulk gap, giving rise to the possibility of multimode edge transport. In our calculations the nontopological edge modes are mostly localized on one of the edges because we have used particular edge terminations, determined by Eq. (10), in the construction of the ribbons. The dependence on the termination highlights the nontopological nature of the edge modes, but in real materials the edges are not expected to be perfectly ordered, and therefore we expect that the nontopological edge modes are distributed on both edges. In fact, for another stacking direction we indeed find that the edge states appear on both sides of the system (see Appendix C). The rest of the paper is devoted to the understanding of the microscopic origin and the other properties of the nontopological edge states.

III. MINIMAL MODEL

In order to understand the microscopic origin of the nontopological edge modes, in this section we consider a model for a buckled honeycomb lattice of anions and cations, which can be considered to be the minimal building block for constructing HgTe/CdTe, HgS/CdTe, and InAs/GaSb heterostructures. We note that this minimal model supports flat bands with nontrivial quantum geometry that gives rise to polarization charges at the edges [20]. In Sec. IV we demonstrate that the polarization charges transform into additional edge states when the flat bands are coupled to each other and to the other states to form the Hamiltonian describing the full heterostructure.

The minimal model can obtained from the full three-dimensional Hamiltonian [Eq. (1)] by projecting the model to

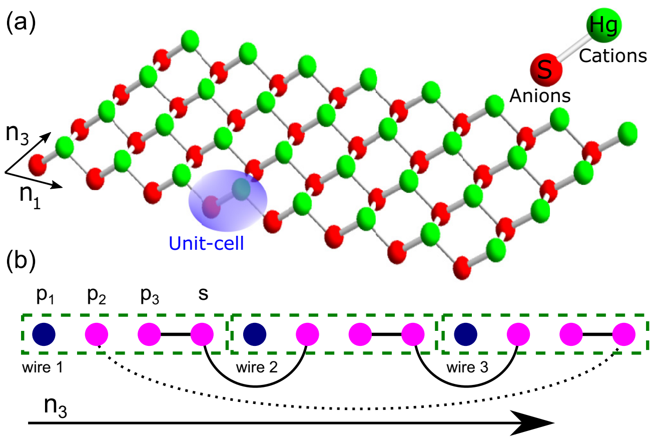

FIG. 6. (a) Buckled honeycomb lattice of anions (red) and cations (green) describing the minimal model. The directions in this two-dimensional system correspond to n_1 and n_3 in the original three-dimensional model [Eq. (1)]. (b) The Zak phases of the flat bands of the model give rise to an accumulated end charge proportional to the width of the ribbon W because of an additional symmetry that allows for the decomposition of the Hamiltonian into diagonal blocks. Each dashed rectangle represents four states, labeled as p_1, p_2, p_3, and s due to their orbital contents, of a single zigzag chain. The states represented by purple (blue) disks form 3×3 (1×1) diagonal blocks after decomposition. The black lines indicate that the states connected by them go to the same block. The dashed black line denotes a coupling, which is present only in the cylinder geometry with periodic boundary conditions in the transverse direction.

s orbitals of cations and p orbitals of anions, neglecting the spin-orbit coupling terms and setting $k_2=\pi$. Furthermore, we set $E_f=0$ for simplicity. This way we obtain a buckled honeycomb lattice shown in Fig. 6(a). The 2D bulk Hamiltonian of this system is

$$\mathcal{H}^{\mathrm{2D}}(k_1,k_3)=H_\parallel(k_1)+(e^{ik_3}H_\perp+\mathrm{H.c.}), \tag{13}$$

and the 1D Hamiltonian of a W unit cells wide ribbon is

$$\mathcal{H}^{\mathrm{1D}}(k_1)=\mathbb{1}_W\otimes H_\parallel(k_1)+(D\otimes H_\perp+\mathrm{H.c.}), \tag{14}$$

where

$$\frac{H_\parallel(k_1)}{E_0}=\begin{pmatrix}\eta_s & e^{ik_1}-1 & -e^{ik_1}+1 & -e^{ik_1}-1\\ e^{-ik_1}-1 & \eta_p & 0 & 0\\ -e^{-ik_1}+1 & 0 & \eta_p & 0\\ -e^{-ik_1}-1 & 0 & 0 & \eta_p\end{pmatrix},$$

$$\frac{H_\perp}{E_0}=\begin{pmatrix}0&2&2&0\\0&0&0&0\\0&0&0&0\\0&0&0&0\end{pmatrix},\ E_0=\frac{V_{s_cp_a\sigma}}{\sqrt{3}},\ \eta_s=\frac{V_{s_c}}{E_0},\ \eta_p=\frac{V_{p_a}}{E_0}.$$

Here, D is a $W\times W$ matrix of the form (11). If we assume a periodic boundary condition in the transverse direction, corresponding to a cylinder geometry instead of a ribbon, the matrix D is replaced by

$$T=\sum_{i=1}^{W-1}|i\rangle\langle i+1|+|W\rangle\langle 1|=D+|W\rangle\langle 1|. \tag{15}$$

The spectrum of $\mathcal{H}(k_1,k_3)$ is flat in the direction of k_3 and there are two completely flat bands,

$$\begin{aligned}E_{1,2}(k_1)&=\tfrac{1}{2}\Big[\eta_p+\eta_s\mp\sqrt{56+(\eta_p-\eta_s)^2-8\cos k_1}\Big],\\ E_3&=E_4=\eta_p.\end{aligned} \tag{16}$$

According to our knowledge the Hamiltonian $\mathcal{H}(k_1,k_3)$ is topologically trivial in all classifications. Nevertheless, we find end states, evolving from the dispersive states $|E_1(k_1)\rangle$ and $|E_2(k_1)\rangle$, when the system is finite along the k_1 direction. The end states are localized on one end of the system and they can be constructed analytically using the non-Bloch wave ansatz described in Ref. [22] (see Appendix D). The charge density of the end states has a decay length

$$\xi=\frac{1}{2\ln 3}, \tag{17}$$

and the energies of the end states are given by

$$E_{1,2}(-i\ln 3)=\frac{1}{2}\left(\eta_p+\eta_s\mp\sqrt{\frac{128}{3}+(\eta_p-\eta_s)^2}\right). \tag{18}$$

Importantly, we obtain these end states with the same energies $E_{1(2)}$ and localization length ξ for all values of k_3 so that the number of end modes is proportional to the width W of the ribbon. The existence of the end modes depends on the lattice termination, so that with the termination used in Appendix D all of the end modes are localized at the right end of the system.

The non-Bloch wave ansatz [22] tells us that there cannot be end states evolving from the flat bands E_3 and E_4, because the energies generically must be of the form $E_n(q)$ with some complex q, so that the flat bands cannot give rise to a state of energy different than η_p. However, the flat bands can still lead to a charge accumulation at the ends of the system due to the Zak phase [20]. Typically, such a kind of quantum geometric effect on the charge accumulation is small because the Zak phase is only defined modulo 2π but we find that in our system the accumulated charge scales with the width W of the ribbon because of an additional symmetry of the system.

Namely, we can transform the ribbon Hamiltonian (14) [and the cylinder Hamiltonian with periodic boundary conditions (15)] as

$$\mathcal{H}^{\mathrm{1D}}(k_1)\to\mathcal{U}^\dagger\mathcal{H}^{1D}(k_1)\mathcal{U},\quad \mathcal{U}=\mathbb{1}_W\otimes U, \tag{19}$$

where

$$U=\begin{pmatrix}0&0&0&1\\ \frac{\cos\frac{k_1}{2}}{\sqrt{3-\cos k_1}} & \frac{1}{\sqrt{2}} & \frac{-i\sin\frac{k_1}{2}e^{-i\frac{k_1}{2}}}{\sqrt{\frac{3-\cos k_1}{2}}} & 0\\ \frac{-\cos\frac{k_1}{2}}{\sqrt{3-\cos k_1}} & \frac{1}{\sqrt{2}} & \frac{i\sin\frac{k_1}{2}e^{-i\frac{k_1}{2}}}{\sqrt{\frac{3-\cos k_1}{2}}} & 0\\ \frac{2i\sin\frac{k_1}{2}}{\sqrt{3-\cos k_1}} & 0 & \frac{-\cos\frac{k_1}{2}e^{-i\frac{k_1}{2}}}{\sqrt{\frac{3-\cos k_1}{2}}} & 0\end{pmatrix}, \tag{20}$$

leading to W identical 1×1 blocks,

$$B_1=E_0(\eta_p), \tag{21}$$

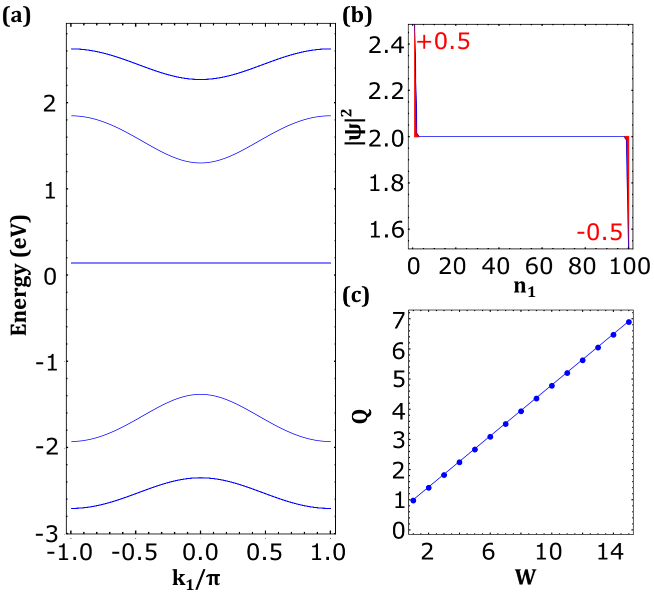

FIG. 7. (a) Band structure of minimal model ribbon of width $W = 8$ unit cells in the $\mathbf{n}_3$ direction. The flat bands have a degeneracy 16, whereas the highest and lowest dispersive bands $E_{1,2}(k_1)$ are sevenfold degenerate and the other dispersive bands $E_{\parallel 1,2}(k_1)$ are nondegenerate. (b) LDOS of flat bands for a single zigzag chain of length $L = 100$ unit cells as a function of position $\mathbf{n}_1$ with the accumulated charge quantized at both ends. (c) Accumulated charge as a function of thickness W along the $\mathbf{n}_3$ direction. We have used $V_{sc} = -1.5535$, $V_{pa} = -1.1909$, $V_{s_c p_a} = 1.1517$, $E_f = -1.330\,27$ (in meV) corresponding to HgS.

$W - 1$ identical 3×3 blocks,

$$B_3 = E_0 \begin{pmatrix} \eta_p & \sqrt{6 - 2\cos k_1} & 0 \\ \sqrt{6 - 2\cos k_1} & \eta_s & \sqrt{8} \\ 0 & \sqrt{8} & \eta_p \end{pmatrix}, \quad (22)$$

and one 3×3 block,

$$B_3' = E_0 \begin{pmatrix} \eta_p & \sqrt{6 - 2\cos k_1} & 0 \\ \sqrt{6 - 2\cos k_1} & \eta_s & c\sqrt{8} \\ 0 & c\sqrt{8} & \eta_p \end{pmatrix},$$

where $c = 0$ ($c = 1$) for the ribbon (cylinder) geometry. A schematic view of how the different states, represented by the columns of matrix U, contribute to each block is shown in Fig. 1(b). Each of the B_3 blocks contains one flat band with energy η_p and two bands with energies $E_{1,2}(k_1)$ given in Eq. (16). In the cylinder geometry with $c = 1$, block B_3' is identical to B_3, but in the ribbon geometry with $c = 0$ the block B_3' contributes a flat band with energy η_p and two dispersive bands with energies

$$E_{\parallel 1,2}(k_1) = \tfrac{1}{2}\left[\eta_p + \eta_s \mp \sqrt{24 + (\eta_p - \eta_s)^2 - 8\cos k_1}\right]. \quad (23)$$

The energy bands of a ribbon with $c = 0$ are shown in Fig. 7(a). Every B_3 block and B_3' block with $c = 1$ contributes two end states with energies $E_{1,2}(-i \ln 3)$ if the system is opened in the k_1 direction, whereas B_3' with $c = 0$ contributes two end states with energies $E_{\parallel 1,2}(-i \ln 3)$.

Because of the block decomposition the accumulated charge at the end of the ribbon, when it is opened in the k_1 direction, is related to the sum of the Zak phases of the different blocks. From an explicit calculation, using the standard prescription

$$\gamma_p = \frac{1}{i} \int_0^{2\pi} \langle E_p(k) | \partial_k | E_p(k) \rangle \quad (24)$$

and the analytical form of the eigenvectors, we get that the Zak phases of the flat bands from the blocks $\{B_1, B_3, B_3'\}$ are

$$\gamma_1 = \pi, \quad \gamma_3 = -\frac{\pi}{\sqrt{3}}, \quad \gamma_3' = -c\frac{\pi}{\sqrt{3}}. \quad (25)$$

Thus, inspired by Ref. [20], we expect that the difference of the left and right boundary charges due to the geometric phases of the flat bands is

$$Q = \frac{1}{\pi}(W\gamma_1 + [W - 1]\gamma_3 + \gamma_3'). \quad (26)$$

Indeed, we numerically find that

$$Q = \begin{cases} \frac{1}{\sqrt{3}} + W\left(1 - \frac{1}{\sqrt{3}}\right), & c = 0, \\ W\left(1 - \frac{1}{\sqrt{3}}\right), & c = 1, \end{cases} \quad (27)$$

demonstrating that Eq. (26) correctly describes the accumulated boundary charge, which increases proportionally to the width W of the system [see Figs. 7(b) and 7(c)].

Note that the above considerations are valid also when we set $k_1 = \pi$ as a starting point and consider a 2D system in the k_2-k_3 plane leading to a 1D ribbon or cylinder Hamiltonian $\mathcal{H}^{1\mathrm{D}}(k_2)$ analogous to Eq. (14). Despite both Hamiltonians being apparently quite different, we show in Appendix E that they are related by a unitary transformation in the case of cylinder geometry and differ only in block B_3' in the case of ribbon geometry. In the former case the end states and the number of flat bands are the same as for $\mathcal{H}^{1\mathrm{D}}(k_1)$ whereas in the latter one the number of edge states (flat bands) is smaller by two (larger by two) because of the difference between B_3' blocks (see Appendix E).

IV. CONNECTION BETWEEN THE NONTOPOLOGICAL EDGE STATES AND THE FLAT BANDS IN THE MINIMAL MODEL

Next, we demonstrate that the nontopological edge states indeed originate from the flat bands of the minimal model by interpolating between the Hamiltonians and following the evolution of the edge states.

We first notice that similar nontopological edge states are obtained both in the full heterostructure of $\mathrm{CdTe}_{10}/\mathrm{HgS}_8/\mathrm{CdTe}_{10}$ and in HgS_8 [Figs. 8(a) and 8(b)]. Indeed, by interpolating between coupled $x = 0$ and uncoupled $x = 1$ systems of HgS_8 and CdTe_{10}, as described in Eq. (9), we find that the majority of the edge states at the high-symmetry point $k_1 = \pi$ remains unchanged throughout the evolution [Fig. 8(c)], despite the fact that the coupling has a large impact on the bulk state energies. Moreover, by studying the eigenvectors we conclude that the edge states are located in the HgS system. Therefore, we conclude that the CdTe barriers are not important for understanding the additional edge modes.

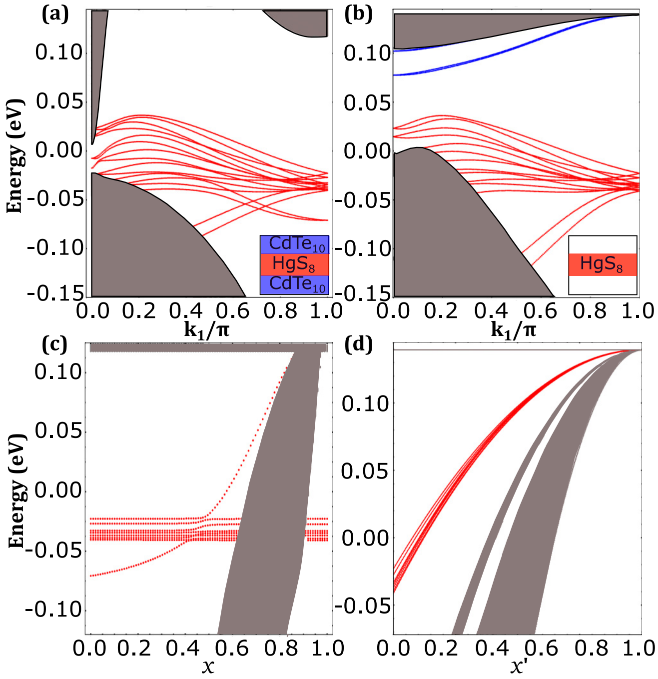

FIG. 8. (a), (b) Edge state spectra of CdTe$_{10}$/HgS$_8$/CdTe$_{10}$ and HgS$_8$ of width $W' = 300$ unit cells in the $\mathbf{n}_2$ direction, respectively. (c) Evolution of eigenenergies at $k_1 = \pi$ as a function of x interpolating between coupled ($x = 0$) and uncoupled ($x = 1$) systems of HgS$_8$ and CdTe$_{10}$ as described in Eq. (9). (d) Evolution of eigenenergies at $k_1 = \pi$ from HgS$_8$ ($x' = 0$) to the minimal model ($x' = 1$).

We can further trace back the origin of additional edge states from the HgS$_8$ system to the minimal model by interpolating the model parameters

$$\vec{P}(x') = (1 - x')\vec{P}_{\text{HgS}} + x'\vec{P}_{\text{min}} \tag{28}$$

between the HgS parameters

$$\vec{P}_{\text{HgS}} = \{V_{s_a}, V_{s_c} V_{p_a}, V_{p_c}, V_{ss\sigma}, \times V_{s_a p_c \sigma}, V_{s_c p_a \sigma}, V_{pp\sigma}, V_{pp\pi}, \lambda_a, \lambda_c, E_f\} \tag{29}$$

and the minimal model parameters

$$\vec{P}_{\text{min}} = \{V_{s_a}, V_{s_c}, V_{p_a}, V_{p_c}, 0, V_{s_c p_a \sigma}, V_{s_a p_c \sigma}, 0, 0, 0, 0, E_f\}. \tag{30}$$

By following the evolution of the edge states of HgS ($x' = 0$) to the minimal model ($x' = 1$) we find that the edge states are indeed connected to the flat bands of the minimal model [see Fig. 8(d)].

V. EFFECT OF EDGE POTENTIAL ON THE NONTOPOLOGICAL EDGE STATES

We have argued that the additional edge states are not topological. This suggests that it should be possible to remove them from the energy gap between the valence and conduction bands by applying an edge potential, for example, with the help of a side gate. In Fig. 9 we show the edge state spectra of CdTe$_{10}$/HgS$_8$/CdTe$_{10}$ in the presence of an additional on-site potential δ applied on the lattice sites at the right edge of the system. By decreasing the value of δ we find that all nontopological edge states can indeed be removed from the bulk gap.

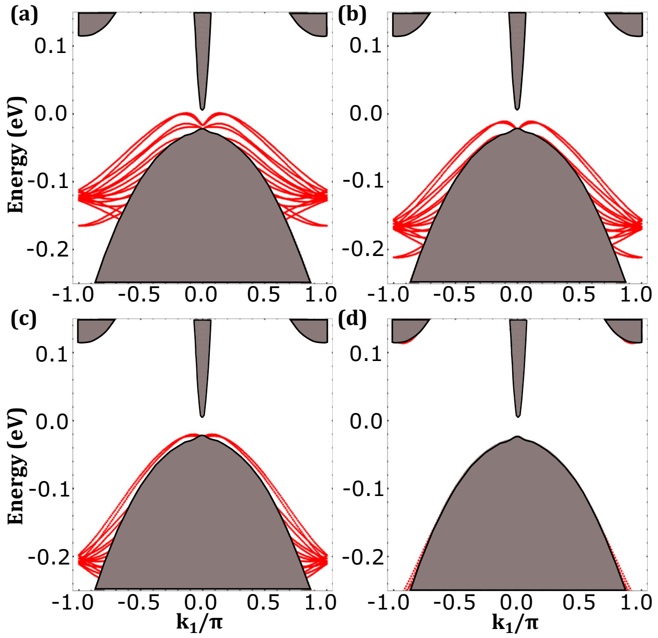

FIG. 9. Edge state spectra of CdTe$_{10}$/HgS$_8$/CdTe$_{10}$ of width $W' = 300$ unit cells with an on-site potential δ applied on the lattice sites at the right edge of the system. The values of the on-site potential are (a) $\delta = -0.1$ eV, (b) $\delta = -0.15$ eV, (c) $\delta = -0.2$ eV, and (d) $\delta = -0.3$ eV.

VI. CONCLUSIONS

We have shown that HgTe/CdTe, HgS/CdTe, and InAs/GaSb heterostructures support additional edge states which are sensitive to edge termination, and we have traced the microscopic origin of these states back to a minimal model supporting flat bands with a nontrivial quantum geometry that gives rise to polarization charges at the edges. Moreover, we expect that additional edge states appear each time the edge cuts the *s*-*p* chains of the minimal model. Nontopological edge states have been observed in quantum spin Hall insulator candidate materials deteriorating the quality of the quantum spin Hall effect. Importantly, our results suggest that these states can be removed from the bulk energy gap by modifying the edge potential, for example, with a side gate or chemical doping.

ACKNOWLEDGMENTS

The research was partially supported by the Foundation for Polish Science through the IRA Programme cofinanced by EU within Smart Growth Operational Programme (Grant No. MAB/2017/1). T.H. acknowledges the computational resources provided by the Aalto Science-IT project and the financial support from the Academy of Finland Project No. 331094. W.B. acknowledges support by Narodowe Centrum Nauki (NCN, National Science Centre, Poland) Project No. 2019/34/E/ST3/00404. R.I. and C.A. acknowledge support by the National Science Center in the framework of the "PRELUDIUM" (Decision No. DEC-2020/37/N/ST3/02338). We acknowledge the access to the computing facilities of the Interdisciplinary Center of Modeling at the University of Warsaw, Grants No. G75-10, No. G84-0, and No. GB84-1. We acknowledge the CINECA award under the ISCRA initiatives IsC93 "RATIO" and IsC99 "SILENTS" grant, for the availability of high-performance computing resources and support.

APPENDIX A: COMPUTATIONAL DETAILS OF THE DENSITY-FUNCTIONAL CALCULATIONS

We performed electronic structure calculations by using the VASP [23] package based on the plane-wave basis set and projector augmented-wave method [24]. A plane-wave energy cutoff of 250 eV has been used. We have performed the calculations using a $8 \times 8 \times 8$ k-point Monkhorst-Pack grid in the presence of SOC with 512 k points and in the absence of SOC with 176 k points in the independent Brillouin zone. For the treatment of exchange correlation, the modified Becke-Johnson exchange potential together with a local density approximation for the correlation potential scheme [25,26] have been considered. In particular, we have an improvement in the band gap [27], and consequently an improvement in the spin-orbit splitting close to the gap. Similar settings for the DFT calculations were used to describe HgTe and InAs [28,29].

After obtaining the Bloch wave functions $\psi_{n,\mathbf{k}}$, the Wannier functions [30,31] are built up using the WANNIER90 code [32]. To extract the low-energy properties of the electronic bands, we have used the Slater-Koster interpolation scheme to obtain a long-range tight-binding model with the Wannier function method [32]. To obtain the first-neighbor tight-binding model, we require the tight-binding model to fit the DFT band structure at the high-symmetry points Γ, X, and L. Regarding the spin orbit, we extracted the effective SOC of the anion λ_a from the formula $3\lambda_a = E(\Gamma_8) - E(\Gamma_7)$, where Γ_8 and Γ_7 anion energy levels were obtained from first-principles calculations [33], and the same was done for the cation λ_c. Note that in Ref. [33] we used a different notation where $\frac{3\lambda_a}{2} = E(\Gamma_8) - E(\Gamma_7)$. Following this procedure, we obtained the hopping parameters, the on-site energies, and the spin-orbit constants. The experimental lattice constants, which coincide with those used in our DFT calculation except for HgS, are reported in Table II. For HgS we have used a larger lattice constant $a_0 = 6.835$ Å to obtain that the effective SOC is close to zero.

We demonstrate why the effective spin-orbit λ_a is negative for the p state of S in HgS [36]. First, we consider a Hamiltonian containing the Hg d states and anion p states with the respective bare SOC defined $\lambda^{\rm bare}_{\text{Hg-}d}$ and $\lambda^{\rm bare}_a$ and we diagonalize the Hamiltonian to calculate the effective spin orbit $\lambda_a \propto E(\Gamma_8) - E(\Gamma_7)$ as a function of the bare parameters. We define the difference between the on-site energies $\Delta\epsilon_1 = V_{pa} - V_{dc} > 0$. We calculate the eigenvalues of the Hamiltonian at the Γ point. In order to evaluate analytically the effective SOC, we perform the Löwdin approximation projecting on the anion subspace, obtaining

$$\lambda_a \approx \lambda_a^{\rm bare} - \frac{H^2_{p_xa,d_{yz}c}\,\lambda^{\rm bare}_{\text{Hg-}d}}{\left(\Delta\epsilon_1 - \frac{3}{2}\lambda^{\rm bare}_{\text{Hg-}d}\right)\left(\Delta\epsilon_1 + \lambda^{\rm bare}_{\text{Hg-}d}\right)}, \qquad \text{(A1)}$$

where $H_{p_xa,d_{yz}c}$ is the matrix element that connects the p_x-a and d_{yz}-c orbitals calculated at the Γ point. If we consider the conditions $|\Delta\epsilon_1| \gg \lambda^{\rm bare}_{\text{Hg-}d}$, we obtain

$$\lambda_a \approx \lambda_a^{\rm bare} - \left(\frac{H_{p_xa,d_{yz}c}}{\Delta\epsilon_1}\right)^2 \lambda_{\text{Hg-}d^{\rm bare}}. \qquad \text{(A2)}$$

We can observe that the leading correction term to the bare spin orbit is always negative. The validity of this formula is restricted to the region close to the Γ point, however, that is the interesting region for this class of compounds. This correction to the bare SOC is present in the entire HgX (X = S, Se, Te) family, however, it is quantitatively more relevant in HgS.

TABLE II. Experimental lattice constant at 8 K for HgTe and at 300 K for HgS, CdTe, at 0 K extrapolation for InAs, GaSb, and AlSb. All the values are in Å.

	HgTe [34]	HgS [34]	CdTe [34]	InAs [35]	GaSb [35]	AlSb [35]
a_0	6.460	5.851	6.480	6.050	6.082	6.128

APPENDIX B: DANGLING BONDS IN DENSITY-FUNCTIONAL CALCULATIONS

Here, we will show how to handle the dangling bonds using density-functional theory in this material class. To do that, we will consider the CdTe$_4$/HgTe$_9$/CdTe$_4$ case that is the most difficult to treat due to the large size of the constituent atoms. Figure 10(a) shows the 2D QW with unsaturated dangling bonds of the anion on top (Te terminated) and the cation on the bottom (Cd terminated). The band structure of the unsaturated crystal structure is shown in Fig. 11(a). We observe a metallic phase due to unsaturated edge states not related to the topology. Due to the large size of Cd and Te atoms, the saturation of the dangling bond with hydrogen atoms does not yield a good effect. To overcome this the dangling bonds of the anions are saturated with sodium atoms and cations are saturated with iodine atoms, as shown in Fig. 10(b). When we saturate the dangling bonds, we recover the band structure of the topological insulator as shown in Fig. 11(b). The 2D QW with these dangling bonds is an insulator by nature with the band inverted at the Γ point if the thickness of HgTe is sufficiently large. After considering the dangling bonds, the tight-binding model gives a satisfactory description of the electronic properties of the system. This saturation refers to the (001) top and bottom surface of the heterostructure and is expected to work similarly for other surfaces.

Additionally, the adatoms could aggregate [37]. Further investigations are needed to establish the results for this case. The necessity to use large unit cells, SOC, and an exchange functional for strongly correlated electrons makes these calculations for adatoms in HgTe quite challenging. Recent results were performed for magnetic bulk impurities in HgTe [33,38],

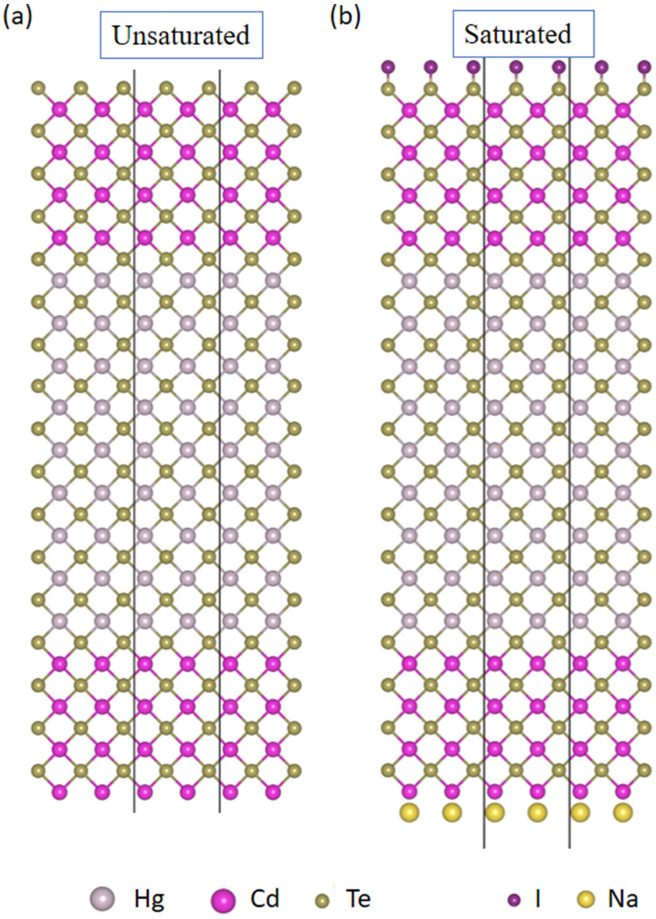

FIG. 10. Crystal structure of the 2D QWs grown along the (001) orientation with (a) unsaturated dangling bonds on the top and bottom surface with stoichiometric concentration. (b) Dangling bond saturated with I and Na on the anion and cation surfaces, respectively.

APPENDIX C: HETEROSTRUCTURES GROWN IN THE (110) DIRECTION

In the main text we have studied heterostructures grown along the direction of the lattice vector $\mathbf{n}_3$. This means that the top and the bottom surfaces are perpendicular to the (001) direction and the side surfaces (edges) are perpendicular to the $(11\bar{1})$ and $(1\bar{1}1)$ directions. However, another typical growth direction of heterostructures is (110). Therefore in this Appendix we check how the results change when we consider this growth direction instead of the one considered in the main text. To address this issue we consider our tight-binding model with the unit cell doubled along the $\mathbf{n}_3$ direction and the new translation vectors being $\mathbf{n}_1' = (1, -1, 0)$, $\mathbf{n}_2' = (1, 1, 0)$, and $\mathbf{n}_3' = (0, 0, 2)$. The layers of the heterostructure are now stacked along $\mathbf{n}_1'$ given the top and bottom surfaces as perpendicular to the (110) direction and the side surfaces or edges perpendicular to the (001) and $(1\bar{1}0)$ directions.

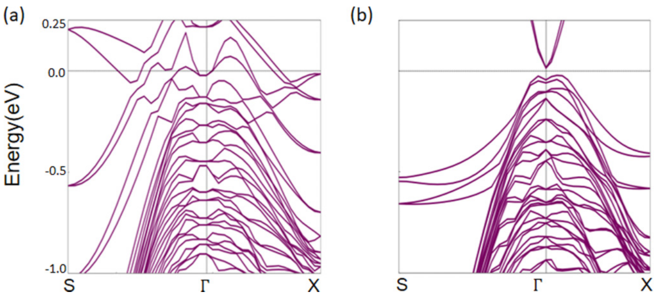

FIG. 11. Band structure of the 2D QWs with (a) unsaturated dangling bonds on the top and bottom surface. (b) Dangling bond saturated with I and Na on the anion and cation surface, respectively. After saturation the DFT band structure resembles the tight-binding Hamiltonian band structure.

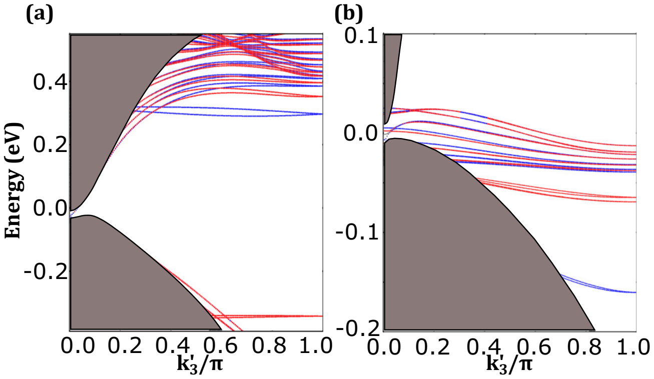

FIG. 12. Edge state spectra for heterostructures grown in the (110) direction: (a) $\mathrm{CdTe}_{10}/\mathrm{HgTe}_{16}/\mathrm{CdTe}_{10}$ and (b) $\mathrm{CdTe}_{10}/\mathrm{HgS}_{8}/\mathrm{CdTe}_{10}$. The widths are $W' = 150$ unit cells in the $\mathbf{n}_2'$ direction.

For these new heterostructures we again construct 2D Hamiltonians $\mathcal{H}^{2\mathrm{D}}(k_2', k_3')$, as in Eq. (5), for which we consider open-edge versions $\mathcal{H}^{1\mathrm{D}}(k_3')$, as in Eq. (10), to verify the presence of the additional edge states at the $(1\bar{1}0)$ surface of the system. As previously, we define W' as a width of the 1D ribbon described by $\mathcal{H}^{1\mathrm{D}}_{k_3'}$. As we can see from the spectra shown in Fig. 12, we still find additional edge states in the HgTe/CdTe and HgS/CdTe heterostructure. Additional edge states of CdTe/HgTe/CdTe lie outside the band gap, whereas for the CdTe/HgS/CdTe heterostructure they appear inside the gap and there is an equal number of them on both edges, in contrast to the cases discussed in the main text.

APPENDIX D: ANALYTICAL DERIVATION OF THE END STATE ENERGIES AND WAVE FUNCTIONS

In this Appendix we calculate the eigenenergies and the wave functions for the end states of the minimal model Hamiltonian (13), when the system has a finite length L along the k_1 direction. By using the Fourier decomposition

$$\mathcal{H}(k_1, k_3) = H_0(k_3) + e^{ik_1}H_1(k_3) + e^{-ik_1}H_1^\dagger(k_3), \tag{D1}$$

the Hamiltonian for the system can be written as

$$\mathcal{H}^{1\mathrm{D}}(k_3) = \mathbb{1}_L \otimes H_0(k_3) + D \otimes H_1(k_3) + D^\intercal \otimes H_1^\dagger(k_3), \tag{D2}$$

where D is the $L \times L$ matrix of the form (11). The eigenstates $|\psi\rangle = \sum_{j=1}^{L} |j\rangle \otimes |\phi_j\rangle$, where $|j\rangle$ is the basis state describing the jth unit cell along the k_1 direction and $|\phi_j\rangle$ is the spinor describing the state within the unit cell, must satisfy

$$H_1^\dagger(k_3)|\phi_{j-1}\rangle + H_0(k_3)|\phi_j\rangle + H_1(k_3)|\phi_{j+1}\rangle = E|\phi_j\rangle, \quad \text{(D3)}$$

for $j = 2, 3, \ldots, L-1$ and the boundary equations

$$\begin{aligned} H_0(k_3)|\phi_1\rangle + H_1(k_3)|\phi_2\rangle &= E|\phi_1\rangle, \\ H_1^\dagger(k_3)|\phi_{L-1}\rangle + H_0(k_3)|\phi_L\rangle &= E|\phi_L\rangle. \end{aligned} \quad \text{(D4)}$$

We write an ansatz for the end states ($n = 1, 2$) as

$$|\phi_{n,j}(q)\rangle = A_q e^{ijq}|E_n(q)\rangle + B_q e^{-ijq}|E_n(-q)\rangle,$$

where the energies

$$E_{1(2)}(q) = \tfrac{1}{2}[\eta_p + \eta_s \mp \sqrt{56 + (\eta_p - \eta_s)^2 - 8\cos q}]. \quad \text{(D5)}$$

and spinors $|E_{1(2)}(q)\rangle$ are obtained from the dispersive bulk states by replacing the momentum k_1 with q. Therefore, the ansatz automatically satisfies Eq. (D3). Importantly, here q is an imaginary number so that the ansatz describes a state localized at the end of the system. Note that $|\phi_{n,j}(q)\rangle$ also contains dependence on k_3 which is however not essential here. Using the boundary conditions we find in the thermodynamic limit $L \to \infty$ for both $n = 1, 2$ and any k_3 that $q = -i\ln 3$ so that the charge density has a decay length

$$\xi = \frac{1}{2\log 3}. \quad \text{(D6)}$$

All end states localized at the right end of the system, and their energies are

$$E_{1(2)}(-i\ln 3) = \frac{1}{2}\left(\eta_p + \eta_s \mp \sqrt{\frac{128}{3} + (\eta_p - \eta_s)^2}\right). \quad \text{(D7)}$$

APPENDIX E: k_1-k_2 DUALITY OF THE MINIMAL MODEL

Consider the minimal model obtained as in Sec. III. Now, instead of setting $k_2 = \pi$ we take $k_1 = \pi$. The 2D bulk Hamiltonian of this system is

$$\mathcal{H}^{2D}(k_2, k_3) = \tilde{H}_\parallel + [e^{ik_3}\tilde{H}_\perp(k_2) + \text{H.c.}], \quad \text{(E1)}$$

and its spectrum does not depend again on k_3. The 1D Hamiltonian of the W unit cell wide cylinder ($c = 1$) is

$$\mathcal{H}^{1D}_{c=1}(k_2) = \mathbb{1}_W \otimes \tilde{H}_\parallel + [T \otimes \tilde{H}_\perp(k_2) + \text{H.c.}], \quad \text{(E2)}$$

which we will compare to the previous case of the $k_2 = \pi$ Hamiltonian,

$$\mathcal{H}^{1D}_{c=1}(k_1) = \mathbb{1}_W \otimes H_\parallel(k_1) + (T \otimes H_\perp + \text{H.c.}). \quad \text{(E3)}$$

Here, T is defined by Eq. (15), $H_\parallel(k_1)$ and $H_\perp$ are defined in Sec. III, and

$$\frac{\tilde{H}_\parallel}{E_0} = \begin{pmatrix} \eta_s & -2 & 2 & 0 \\ -2 & \eta_p & 0 & 0 \\ 2 & 0 & \eta_p & 0 \\ 0 & 0 & 0 & \eta_p \end{pmatrix}, \quad \text{(E4)}$$

and

$$\frac{\tilde{H}_\perp(k_2)}{E_0} = \begin{pmatrix} 0 & -e^{-ik_2}+1 & -e^{-ik_2}+1 & e^{-ik_2}+1 \\ 0 & 0 & 0 & 0 \\ 0 & 0 & 0 & 0 \\ 0 & 0 & 0 & 0 \end{pmatrix}. \quad \text{(E5)}$$

By a close inspection of the 1D chains described by the Hamiltonians (E2) and (E3) we find a duality relation between these two Hamiltonians given by

$$\mathcal{H}^{1D}_{c=1}(k_1) = \mathcal{V}^\dagger \mathcal{H}^{1D}_{c=1}(k_2 = -k_1)\mathcal{V}, \quad \text{(E6)}$$

where $\mathcal{V}$ is a unitary operator,

$$\mathcal{V} = \begin{cases} P_3P_2P_1GQ, & W \in 2\mathbb{N}+1, \\ P_3P_2P_1G, & W \in 2\mathbb{N}. \end{cases} \quad \text{(E7)}$$

Here, $P_{1,2,3}$ are the site permutations,

$$P_1 = \mathbb{1}_W \otimes \begin{pmatrix} 0 & 1 & 0 & 0 \\ 0 & 0 & 1 & 0 \\ 0 & 0 & 0 & 1 \\ 1 & 0 & 0 & 0 \end{pmatrix}, \quad \text{(E8)}$$

$$P_2 = \begin{pmatrix} 0 & \cdots & 0 & 0 & 0 & 1 & 0 \\ 0 & \cdots & 0 & 0 & 1 & 0 & 0 \\ 0 & \cdots & 0 & 1 & 0 & 0 & 0 \\ \vdots & \vdots & \vdots & \vdots & \vdots & \vdots & \vdots \\ 0 & 1 & 0 & 0 & \cdots & 0 & 0 \\ 1 & 0 & 0 & 0 & \cdots & 0 & 0 \\ 0 & 0 & 0 & 0 & \cdots & 0 & 1 \end{pmatrix}, \quad \text{(E9)}$$

and

$$P_3 = \mathbb{1}_W \otimes \begin{pmatrix} 0 & 0 & 0 & 1 \\ 0 & 1 & 0 & 0 \\ 0 & 0 & 1 & 0 \\ 1 & 0 & 0 & 0 \end{pmatrix}. \quad \text{(E10)}$$

Note that P_1 and P_3 only reshuffle sites inside the unit cell consisting of four sites whereas the order of the unit cells remains unchanged. On the other hand, the P_2 operator reverts the whole chain and shifts sites by one in a cyclic manner. The remaining constituents of $\mathcal{V}$ are the alternating gauge matrix,

$$G = \begin{pmatrix} 1 & 0 & 0 & 0 & \cdots \\ 0 & -1 & 0 & 0 & \\ 0 & 0 & 1 & 0 & \\ 0 & 0 & 0 & -1 & \\ \vdots & & & & \ddots \end{pmatrix} \otimes \begin{pmatrix} 1 & 0 & 0 & 0 \\ 0 & -1 & 0 & 0 \\ 0 & 0 & 1 & 0 \\ 0 & 0 & 0 & -1 \end{pmatrix}, \quad \text{(E11)}$$

and operator Q acting on the first unit cell,

$$Q = \begin{pmatrix} 1 & 0 & 0 & \cdots & 0 \\ 0 & 0 & 0 & \cdots & 0 \\ 0 & 0 & 0 & \cdots & 0 \\ \vdots & \vdots & \vdots & \vdots & \vdots \\ 0 & 0 & 0 & \cdots & 0 \end{pmatrix} \otimes \begin{pmatrix} 1 & 0 & 0 & 0 \\ 0 & 0 & -1 & 0 \\ 0 & -1 & 0 & 0 \\ 0 & 0 & 0 & 1 \end{pmatrix} + \begin{pmatrix} 0 & 0 & 0 & 0 & \cdots & 0 \\ 0 & 1 & 0 & 0 & \cdots & 0 \\ 0 & 0 & 1 & 0 & \cdots & 0 \\ \vdots & \vdots & \vdots & \vdots & \vdots & \vdots \\ 0 & 0 & \cdots & 0 & 1 & 0 \\ 0 & 0 & 0 & \cdots & 0 & 1 \end{pmatrix} \otimes \mathbb{1}_4. \quad \text{(E12)}$$

From Eq. (E6) and the results of Sec. III it follows that for a cylindrical geometry along k_3 the $\mathcal{H}^{1D}_{c=1}(k_2)$ Hamiltonian splits into W identical 1×1 blocks,

$$\tilde{B}_1 = E_0(\eta_p), \quad \text{(E13)}$$

and another W identical 3×3 blocks,

$$\tilde{B}_3 = E_0 \begin{pmatrix} \eta_p & \sqrt{6-2\cos k_2} & 0 \\ \sqrt{6-2\cos k_2} & \eta_s & \sqrt{8} \\ 0 & \sqrt{8} & \eta_p \end{pmatrix}, \tag{E14}$$

under transformation $\mathcal{W} = V\,U$. The same transformation $\mathcal{W}$ used on a ribbon-geometry ($c = 0$) Hamiltonian

$$\tilde{\mathcal{H}}^{\rm 1D}_{c=0}(k_2) = \mathbb{1}_W \otimes \tilde{H}_\parallel + [D \otimes \tilde{H}_\perp(k_2) + \text{H.c.}], \tag{E15}$$

with D defined by Eq. (11) gives almost the same block structure with one of the 3×3 blocks substituted by

$$\tilde{B}'_3 = E_0 \begin{pmatrix} \eta_p & 0 & 0 \\ 0 & \eta_s & \sqrt{8} \\ 0 & \sqrt{8} & \eta_p \end{pmatrix}. \tag{E16}$$

Concluding, we have found that for cylindrical geometry the Hamiltonians $\mathcal{H}^{\rm 1D}_{c=1}(k_1)$ and $\tilde{\mathcal{H}}^{\rm 1D}_{c=1}(k_2)$ have the same band structures and the same end states. In the case of the ribbon geometry $\tilde{\mathcal{H}}^{\rm 1D}_{c=0}(k_2)$ has two more (less) flat (dispersive) bands compared to $\mathcal{H}^{\rm 1D}_{c=0}(k_1)$, following from the difference between blocks $\tilde{B}'_3$ and B'_3. The number of end states in this case is smaller by two because the $\tilde{B}'_3$ having no dispersion cannot contribute any, unlike B'_3.

[1] M. Z. Hasan and C. L. Kane, Colloquium: Topological insulators, Rev. Mod. Phys. **82**, 3045 (2010).

[2] X.-L. Qi and S.-C. Zhang, Topological insulators and superconductors, Rev. Mod. Phys. **83**, 1057 (2011).

[3] B. A. Bernevig, T. L. Hughes, and S.-C. Zhang, Quantum spin Hall effect and topological phase transition in HgTe quantum wells, Science **314**, 1757 (2006).

[4] C. Liu, T. L. Hughes, X.-L. Qi, K. Wang, and S.-C. Zhang, Quantum Spin Hall Effect in Inverted Type-II Semiconductors, Phys. Rev. Lett. **100**, 236601 (2008).

[5] M. König, S. Wiedmann, C. Brüne, A. Roth, H. Buhmann, L. W. Molenkamp, X.-L. Qi, and S.-C. Zhang, Quantum spin Hall insulator state in HgTe quantum wells, Science **318**, 766 (2007).

[6] L. Du, I. Knez, G. Sullivan, and R.-R. Du, Robust Helical Edge Transport in Gated InAs/GaSb Bilayers, Phys. Rev. Lett. **114**, 096802 (2015).

[7] S. Wu, V. Fatemi, Q. D. Gibson, K. Watanabe, T. Taniguchi, R. J. Cava, and P. Jarillo-Herrero, Observation of the quantum spin Hall effect up to 100 kelvin in a monolayer crystal, Science **359**, 76 (2018).

[8] L. Lunczer, P. Leubner, M. Endres, V. L. Müller, C. Brüne, H. Buhmann, and L. W. Molenkamp, Approaching Quantization in Macroscopic Quantum Spin Hall Devices through Gate Training, Phys. Rev. Lett. **123**, 047701 (2019).

[9] Y. Tanaka, A. Furusaki, and K. A. Matveev, Conductance of a Helical Edge Liquid Coupled to a Magnetic Impurity, Phys. Rev. Lett. **106**, 236402 (2011).

[10] J. C. Budich, F. Dolcini, P. Recher, and B. Trauzettel, Phonon-Induced Backscattering in Helical Edge States, Phys. Rev. Lett. **108**, 086602 (2012).

[11] A. M. Lunde and G. Platero, Helical edge states coupled to a spin bath: Current-induced magnetization, Phys. Rev. B **86**, 035112 (2012).

[12] A. Del Maestro, T. Hyart, and B. Rosenow, Backscattering between helical edge states via dynamic nuclear polarization, Phys. Rev. B **87**, 165440 (2013).

[13] D. I. Pikulin and T. Hyart, Interplay of Exciton Condensation and the Quantum Spin Hall Effect in InAs/GaSb Bilayers, Phys. Rev. Lett. **112**, 176403 (2014).

[14] T. Paul, V. Fernández Becerra, and T. Hyart, Interplay of quantum spin Hall effect and spontaneous time-reversal symmetry breaking in electron-hole bilayers. I. Transport properties, Phys. Rev. B **106**, 235420 (2022).

[15] J. I. Väyrynen, M. Goldstein, Y. Gefen, and L. I. Glazman, Resistance of helical edges formed in a semiconductor heterostructure, Phys. Rev. B **90**, 115309 (2014).

[16] T. Dietl, Charge dopants control quantum spin Hall materials, arXiv:2206.01613.

[17] G. Dolcetto, M. Sassetti, and T. L. Schmidt, Edge physics in two-dimensional topological insulators, Riv. Nuovo Cimento **39**, 113 (2016).

[18] F. Nichele, H. J. Suominen, M. Kjaergaard, C. M. Marcus, E. Sajadi, J. A. Folk, F. Qu, A. J. A. Beukman, F. K. de Vries, J. van Veen, S. Nadj-Perge, L. P. Kouwenhoven, B.-M. Nguyen, A. A. Kiselev, W. Yi, M. Sokolich, M. J. Manfra, E. M. Spanton, and K. A. Moler, Edge transport in the trivial phase of InAs/GaSb, New J. Phys. **18**, 083005 (2016).

[19] M. C. Dartiailh, S. Hartinger, A. Gourmelon, K. Bendias, H. Bartolomei, H. Kamata, J.-M. Berroir, G. Fève, B. Plaçais, L. Lunczer, R. Schlereth, H. Buhmann, L. W. Molenkamp, and E. Bocquillon, Dynamical Separation of Bulk and Edge Transport in HgTe-Based 2D Topological Insulators, Phys. Rev. Lett. **124**, 076802 (2020).

[20] J.-W. Rhim, J. Behrends, and J. H. Bardarson, Bulk-boundary correspondence from the intercellular Zak phase, Phys. Rev. B **95**, 035421 (2017).

[21] W.-K. Lou, W. Yang, and K. Chang, Helical conducting edge states in narrow-gap semiconductors without band inversion, Phys. Rev. B **105**, 045305 (2022).

[22] K. Yokomizo and S. Murakami, Non-Bloch Band Theory of Non-Hermitian Systems, Phys. Rev. Lett. **123**, 066404 (2019).

[23] G. Kresse and J. Furthmüller, Efficiency of ab-initio total energy calculations for metals and semiconductors using a plane-wave basis set, Comput. Mater. Sci. **6**, 15 (1996).

[24] G. Kresse and D. Joubert, From ultrasoft pseudopotentials to the projector augmented-wave method, Phys. Rev. B **59**, 1758 (1999).

[25] A. D. Beckea and E. R. Johnson, A simple effective potential for exchange, J. Chem. Phys. **124**, 221101 (2006).

[26] F. Tran and P. Blaha, Accurate Band Gaps of Semiconductors and Insulators with a Semilocal Exchange-Correlation Potential, Phys. Rev. Lett. **102**, 226401 (2009).

[27] J. A. Camargo-Martínez and R. Baquero, Performance of the modified Becke-Johnson potential for semiconductors, Phys. Rev. B **86**, 195106 (2012).

[28] R. Islam, B. Ghosh, G. Cuono, A. Lau, W. Brzezicki, A. Bansil, A. Agarwal, B. Singh, T. Dietl, and C. Autieri, Topological states in superlattices of HgTe class of materials for engineering three-dimensional flat bands, Phys. Rev. Res. **4**, 023114 (2022).

[29] G. Hussain, G. Cuono, R. Islam, A. Trajnerowicz, J. Jureńczyk, C. Autieri, and T. Dietl, Electronic and optical properties of InAs/InAs$_{0.625}$Sb$_{0.375}$ superlattices and their application to far-infrared detectors, J. Phys. D **55**, 495301 (2022).

[30] N. Marzari and D. Vanderbilt, Maximally localized generalized Wannier functions for composite energy bands, Phys. Rev. B **56**, 12847 (1997).

[31] I. Souza, N. Marzari, and D. Vanderbilt, Maximally localized Wannier functions for entangled energy bands, Phys. Rev. B **65**, 035109 (2001).

[32] A. A. Mostofi, J. R. Yates, Y. S. Lee, I. Souza, D. Vanderbilt, and N. Marzari, WANNIER90: A tool for obtaining maximally-localised Wannier functions, Comput. Phys. Commun. **178**, 685 (2008).

[33] C. Autieri, C. Śliwa, R. Islam, G. Cuono, and T. Dietl, Momentum-resolved spin splitting in mn-doped trivial CdTe and topological HgTe semiconductors, Phys. Rev. B **103**, 115209 (2021).

[34] *Physics of Group II-IV Elements and I-VII Compounds*, edited by O. Madelung, M. Schulz, and H. Weiss, Landolt-Börnstein, New Series, Group III, Vol. 17,Pt. B (Springer, Berlin, 1982).

[35] I. Vurgaftman, J. R. Meyer, and L. R. Ram-Mohan, Band parameters for III-V compound semiconductors and their alloys, J. Appl. Phys. **89**, 5815 (2001).

[36] Q.-Z. Wang, S.-C. Wu, C. Felser, B. Yan, and C.-X. Liu, Spin texture and mirror Chern number in Hg-based chalcogenides, Phys. Rev. B **91**, 165435 (2015).

[37] N. Gonzalez Szwacki, J. A. Majewski, and T. Dietl, Aggregation and magnetism of Cr, Mn, and Fe cations in GaN, Phys. Rev. B **83**, 184417 (2011).

[38] C. Śliwa, C. Autieri, J. A. Majewski, and T. Dietl, Superexchange dominates in magnetic topological insulators, Phys. Rev. B **104**, L220404 (2021).